



1           **Tornado-Scale Vortices in the Tropical Cyclone Boundary Layer:**  
2                           **Numerical Simulation with WRF-LES Framework**

3   Liguang Wu<sup>1,2</sup>, Qingyuan Liu<sup>1</sup> and Yubing Li<sup>1</sup>

4           <sup>1</sup>Pacific Typhoon Research Center and Key Laboratory of Meteorological Disaster of  
5           Ministry of Education, Nanjing University of Information Science and Technology,  
6   Nanjing, China

7           <sup>2</sup>Department of Atmospheric and Oceanic Sciences and Institute of Atmospheric  
8           Sciences, Fudan University, Shanghai, China

9  
10  
11  
12  
13  
14  
15  
16  
17  
18  
19  
20  
21  
22  
23  
24  
25  
26  
27  
28  
29  
30

Corresponding author address: Dr. Liguang Wu  
Pacific Typhoon Research Center  
Nanjing University of Information Science and Technology, Nanjing, Jiangsu 210044  
E-mail: [liguang@nuist.edu.cn](mailto:liguang@nuist.edu.cn)



31 **Abstract**

32 The tornado-scale vortex in the tropical cyclone (TC) boundary layer (TCBL) has been  
33 observed in intense hurricanes and the associated intense turbulence poses a severe threat  
34 to the manned research aircraft when it penetrates hurricane eyewalls at a lower altitude.  
35 In this study, a numerical experiment in which a TC evolves in a large-scale background  
36 over the western North Pacific is conducted using the Advanced Weather Research and  
37 Forecast (WRF) model by incorporating the large eddy simulation (LES) technique. The  
38 simulated tornado-scale vortex shows the similar features as revealed with the limited  
39 observational data, including the updraft/downdraft couplet, the sudden jump of wind  
40 speeds, the favorable location, and the horizontal scale. It is suggested that the WRF-LES  
41 framework can successfully simulate the tornado-scale vortex with the grids at the  
42 resolution of 37 m that cover the TC eye and eyewall.

43 The simulated tornado-scale vortex is a cyclonic circulation with a small horizontal  
44 scale of  $\sim 1$  km in the TCBL. It is accompanied by strong updrafts (more than  $15 \text{ m s}^{-1}$ ) and  
45 large vertical components of relative vorticity (larger than  $0.2 \text{ s}^{-1}$ ). The tornado-scale vortex  
46 favorably occurs at the inner edge of the enhanced eyewall convection or rainband within  
47 the saturated, high- $\theta_e$  layer, mostly below the altitude of 2 km. Nearly in all the simulated  
48 tornado-scale vortices, the narrow intense updraft is coupled with the relatively broad  
49 downdraft, constituting one or two updraft/downdraft couplets or horizontal rolling  
50 vortices, as observed by the research aircraft. The presence of the tornado-scale vortex also  
51 leads to significant gradients in the near surface wind speed and wind gusts.

52



## 53 1. Introduction

54 Tropical cyclones (TCs) pose a severe risk to life and property in TC-prone areas and  
55 the risk will increase due to the rapidly rising coastal population and buildings (Pielke et  
56 al. 2008; Zhang et al. 2009). One of the major TC threats is damaging winds. Uneven  
57 damage patterns often show horizontal scales ranging from a few hundred meters to several  
58 kilometers (Wakimoto and Black 1994; Wurman and Kosiba 2018), suggesting that TC  
59 threats are associated with both sustained winds and gusts. The latter are believed to result  
60 from small-scale coherent structures in the TC boundary layer (Wurman and Winslow 1998;  
61 Morrison et al. 2005; Lorsolo et al. 2008; Kosiba et al. 2013; Kosiba and Wurman 2014).  
62 The small-scale coherent structures may have significant implications for the vertical  
63 transport of energy in TCs and thus TC intensity and structure (Zhu 2008; Rotunno et al.  
64 2009; Zhu et al. 2013; Green and Zhang 2014, 2015; Gao et al. 2017). While understanding  
65 of the coherent structure is very important for mitigating TC damage and understanding of  
66 TC intensity and structure changes, by now direct in situ observation and remote sensing  
67 measurements can only provide very limited information.

68 In the TC boundary layer (TCBL), observational analyses suggest that horizontal  
69 streamwise roll vortices prevail with sub-kilometer to multi-kilometer wavelengths  
70 (Wurman and Winslow 1998; Katsaros et al. 2002; Morrison et al. 2005; Lorsolo et al.  
71 2008; Ellis and Businger 2010; Foster, 2013). Studies found that the rolls can result from  
72 the inflection point instability of the horizontal wind profiles in the TCBL (Foster 2005;  
73 Gao and Ginis 2014) and have significant influences on the vertical transport of energy in  
74 TCs (Zhu 2008; Rotunno et al. 2009; Zhu et al. 2013; Green and Zhang 2014, 2015; Gao  
75 et al. 2017). The TCBL is known to play a critical role in transporting energy and



76 controlling TC intensity (Braun and Tao 2000; Rotunno et al. 2009; Smith and  
77 Montgomery 2010; Bryan 2012; Zhu et al. 2013; Green and Zhang 2015).

78 Another important small-scale feature is the so-called eyewall vorticity maximum  
79 (EVM) (Marks et al. 2008) or tornado-scale vortices in the TCBL (Wurman and Kosiba  
80 2018; Wu et al. 2018). So far, our understanding is mainly from a few observational  
81 analyses based on limited data collected during the research aircraft penetration of  
82 hurricane eyewalls. A WP-3D research aircraft from National Oceanic and Atmospheric  
83 Administration (NOAA) encountered three strong updraft-downdraft couplets within one  
84 minute while penetrating the eyewall of category 5 Hurricane Hugo (1989) at 450-m  
85 altitude (Marks et al. 2008). The severe turbulence caused the failure of one of the four  
86 engines and the people aboard were at a severe risk. The aircraft finally escaped with the  
87 help of a U. S. Air Force reconnaissance WC-130 aircraft, which found a safe way out  
88 through the eyewall on the northeast side of Hugo. Since then the aircraft mission has been  
89 prohibited in the boundary layer of the TC eyewall. Later analysis indicated that the  
90 dangerous turbulence was associated with a tornado-scale vortex, which is comparable to  
91 a weak tornado in terms of its diameter of about 1 km and the estimated peak cyclonic  
92 vorticity of  $0.125 \text{ s}^{-1}$  (Marks et al. 2008). Such strong turbulence was also observed in  
93 Hurricanes Isabel (2003) and Felix (2007) at different altitudes (Aberson et al. 2006;  
94 Aberson et al. 2017). Understanding of the structure and evolution of the tornado-scale  
95 vortex is hampered since it is difficult to directly observe due to its small horizontal scale  
96 and the associated severe turbulence.

97 With advances in numerical models and computational capability, the large eddy  
98 simulation (LES) technique has been incorporated into the Advanced Weather Research



99 and Forecast (WRF) model (Mirocha et al. 2010) and an increasing number of TC  
100 simulations have been conducted with horizontal grid spacing less than 1 km (Zhu 2008;  
101 Rotunno et al. 2009; Bryan et al. 2014; Stern and Bryan 2014; Rotunno and Bryan 2014;  
102 Green and Zhang 2015). In LES the energy-producing scales of 3-dimensional (3D)  
103 atmospheric turbulence in the planetary boundary layer (PBL) are explicitly resolved,  
104 while the smaller-scale portion of the turbulence is parameterized (Mirocha et al. 2010).  
105 Effort has been made to simulate the structure of the TC PBL eddies and the associated  
106 influence on TC intensity. Zhu (2008) simulated the structure of the coherent large eddy  
107 circulations and the induced vertical transport using the WRF-LES framework with  
108 horizontal resolutions of 300 m and 100 m. When the horizontal resolution was decreased  
109 from 185 to 62 m on the f-plane, Rotunno et al. (2009) found a sharp increase in randomly  
110 distributed small-scale turbulent eddies, while 1-minute mean TC intensity began to  
111 decrease. Green and Zhang (2015) performed several 6-hour one-way simulations of  
112 Hurricane Katrina (2005) without a boundary layer parameterization (horizontal  
113 resolutions of 333, 200, and 111 m). Rotunno et al. (2009) and Green and Zhang (2015)  
114 suggest that the horizontal resolution should be below 100 m to simulate the development  
115 of 3D turbulent eddies in TCBL.

116 It is clear that understanding of the tornado-scale vortex would enhance the safety of  
117 flights into very intense TCs. In addition, the tornado-scale vortex may be responsible for  
118 TC intensification by mixing the high-entropy air in the eye into the eyewall (Persing and  
119 Montgomery 2003; Montgomery et al. 2006; Aberson et al. 2006) and track fluctuations  
120 (Marks et al. 2008; Aberson et al. 2017). By simulating the tornado-scale vortex in the  
121 TCBL, this study will particularly focus on the spatial distribution of the occurrence of the



122 tornado-scale vortex and the features of its 3D structures.

## 123 **2. The numerical experiment**

124 In this study the numerical simulation is conducted using version 3.2.1 of the WRF  
125 model. Following Wu and Chen (2016), two steps were taken to construct the initial  
126 conditions for the numerical experiment. A symmetric vortex was first spun up without the  
127 environmental flow on an f-plane for 18 hours and then the vortex was embedded in the  
128 large-scale background of Typhoon Matsa (2005) from 0000 UTC 5 August to 1200 UTC  
129 6 August. The large-scale environment was derived from the National Centers for  
130 Environmental Prediction (NCEP) Final (FNL) Operational Global Analysis data with  
131 resolution of  $1.0^\circ \times 1.0^\circ$  using a 20-day low-pass Lanczos filter (Duchon 1979).

132 The spun-up vortex is initially located at the center of Typhoon Matsa ( $25.4^\circ\text{N}$ ,  
133  $123.0^\circ\text{E}$ ). The outermost domain centered at  $30.0^\circ\text{N}$ ,  $132.5^\circ\text{E}$  covers an area of  $6210 \times 6210$   
134  $\text{km}^2$  with a horizontal spacing of 27 km. The numerical experiment is designed with six  
135 two-way interactive domains embedded in the 27-km resolution domain to simulate  
136 energetic 3-dimensional turbulent eddies in the TC eyewall and their influence on the TC  
137 vortex, mesoscale rainbands and convective clouds. The horizontal spacing decreases by a  
138 factor of 3 with the domain level. The corresponding horizontal resolutions are 9 km, 3 km,  
139 1 km,  $1/3$  km (333 m),  $1/9$  km ( $\sim 111$  m) and  $1/27$  km ( $\sim 37$  m) and the numbers of their  
140 grid meshes are  $230 \times 210$ ,  $432 \times 399$ ,  $333 \times 333$ ,  $501 \times 501$ ,  $1351 \times 1351$ , and  $2431 \times 2431$ ,  
141 respectively. The innermost domain covers the inner region of the simulated TC ( $90 \times 90$   
142  $\text{km}^2$ ), including the eye and eyewall. Except the 27-km and 9-km resolution domains, the  
143 other domains move with the TC. The model consists of 75 vertical levels (19 levels below



144 2 km) with a top of 50 hPa and is run over the open ocean with a constant sea surface  
145 temperature 29°C.

146 The physics options used in the simulation are as follows. The Kain-Fritsch cumulus  
147 parameterization scheme and the WRF single-moment 3-class scheme are used in the  
148 outermost domain (Kain and Fritsch 1993). The WRF 6-class scheme is selected in the  
149 nested domains with no cumulus parameterization scheme (Hong and Lim 2006). The  
150 Rapid Radiative Transfer Model (RRTM) and the Dudhia shortwave radiation scheme are  
151 used for calculating long-wave radiation and shortwave radiation (Mlawer et al. 1997;  
152 Dudhia 1989). The LES technique is used in the sub-kilometer domains (Mirocha et al.  
153 2010) and the Yonsei University scheme is adopted for PBL parameterization in the other  
154 domains (Noh et al. 2003).

155 The model is run for 36 hours and the 1/9-km-resolution and 1/27-km-resolution  
156 domains are activated at 24 h. In the following analysis, we will focus on the hourly output  
157 from 26 h to 36 h. The TC center is determined with a variational approach in which it is  
158 located until the maximum azimuthal-mean tangential wind speed is obtained (Wu et al.  
159 2006). A few variables are also stored at 3-second intervals during a 22-minute period from  
160 the 30<sup>th</sup> hour.

### 161 3. The simulated small-scale features

162 The simulated TC takes a northern north west track (figure not shown). Figure 1 shows  
163 its intensity in terms of the instantaneous and azimuthal maximum wind speeds at 10 m in  
164 the 1/27 km-resolution domain. The instantaneous winds are directly from the model  
165 instantaneous output without any time averaging and the azimuthal wind speed is the wind  
166 speed averaged azimuthally with respect to the TC center. The instantaneous maximum



167 wind speed fluctuates between  $76.6 \text{ m s}^{-1}$  and  $61.8 \text{ m s}^{-1}$  during the 12-hour period, while  
168 the fluctuations in the azimuthal maximum wind speed is relatively small, ranging from  
169  $48.8 \text{ m s}^{-1}$  to  $43.5 \text{ m s}^{-1}$ . In particular, the TC maintains the azimuthal mean maximum wind  
170 speed of  $\sim 45 \text{ m s}^{-1}$  after the innermost domain has been activated for two hours.

171 Figure 2a shows the simulated 500-m radar reflectivity at 27 h, indicating that the  
172 eyewall is open to the south of the TC center. We examine the radar reflectivity field and  
173 find that the opened eyewall persists during the 10-hour period. In addition, the location of  
174 the enhanced convection relative to the TC center is generally steady. It is well known that  
175 the eyewall asymmetry is associated with the vertical shear of the environmental flow  
176 (Frank and Ritchie 2001, Braun and Wu 2007). In this study the vertical wind shear  
177 calculated as the difference of wind vectors between 200 hPa and 850 hPa within a radius  
178 of 300 km. As shown in the figure, the mean shear is  $5.2 \text{ m s}^{-1}$  to the southeast over the 10-  
179 hour period. In agreement with the previous studies, the enhanced eyewall reflectivity is  
180 generally observed in the downshear left side. There are relatively small changes in the  
181 RMW during the 11-hour period, ranging from 28.2 km to 30.7 km at 500 m.

182 Using the fine-scale dual Doppler data in the right front quadrant and eye of Hurricane  
183 France (2004) as it made landfall on Florida, Kosiba and Wurman (2014) found linear  
184 coherent structures with a wavelength of 400-500 m near the surface. Figure 2b shows the  
185 simulated near-surface (10 m) wind speeds in the inner region at 27 h. The instantaneous  
186 wind speed is dominated by quasi-linear coherent structures in the eyewall region. The  
187 intense instantaneous wind speeds coincide with the enhanced eyewall convection shown  
188 in Figure 2a. In order to show clearly the quasi-linear feature, we plot the instantaneous  
189 wind speed in an area of  $7 \times 10 \text{ km}^2$  at this time (Fig. 3a). The small area is located in the





190 eyewall to the east of the TC center (Fig. 2b). The streaks of alternating high and low wind  
191 speeds can be clearly seen, which are roughly aligned with the TC-scale flow with an  
192 outward angle. We can see that the instantaneous wind speed exhibits large gradients across  
193 the quasi-linear structures.

194 Figure 3b shows the perturbation wind field at 500 m in the small area. The perturbation  
195 winds are obtained by subtracting an 8-km moving mean. We compare the perturbation  
196 winds with different sizes of the moving window. While the perturbation wind fields are  
197 very similar, the wind speeds generally increase with the increasing window size. When  
198 the window size is larger than 8 km, there is little change in the perturbation wind speed. The  
199 results are similar to those by subtracting the symmetric and wavenumber 1-3 components  
200 with respect to the TC center. In the perturbation wind field, we can see two small-scale  
201 cyclonic circulations. The most distinct one has a diameter of ~2 km. In the next section,  
202 the two cyclones are identified as two tornado-scale vortices (M2701 and M2705).  
203 Compared to Figure 3a, the two tornado-scale vortices also correspond to enhanced wind  
204 speeds at 10 m.

#### 205 4. Identification of EVMs

206 As mentioned in Section 1, analyses of a few real cases in Atlantic intense hurricanes  
207 indicate that the tornado-scale vortex is a small-scale feature that occurs in the turbulent  
208 TC boundary, with vertical motion and relative vorticity extremes. Aberson et al. (2006)  
209 and Aberson et al. (2016) analyzed the extreme updrafts in Hurricanes Isabel (2003) and  
210 Felix (2007) and suggested that the strong updrafts were likely associated with the tornado-  
211 scale vortex. The updraft of  $25 \text{ m s}^{-1}$  in Isabel was detected by a GPS dropwindsonde just  
212 below 800 hPa, while the updraft of  $31 \text{ m s}^{-1}$  in Hurricane Felix (2007) was observed at the



213 flight altitude ( $\sim 3$  km). Marks et al. (2008) found that the tornado-scale vortex in Hurricane  
214 Hugo (1989) was associated with a maximum vertical motion of  $21 \text{ m s}^{-1}$  and a maximum  
215 relative vorticity of  $0.125 \text{ s}^{-1}$  at the altitude of 450 m. Based on these studies, the tornado-  
216 scale vortex in the simulated TC is defined as a small-scale cyclonic circulation with the  
217 diameter of 1-2 km below the altitude of 3 km, containing maximum upward motion larger  
218 than  $20 \text{ m s}^{-1}$  and maximum relative vorticity larger than  $0.2 \text{ s}^{-1}$ . The grid points that satisfy  
219 the thresholds of vertical motion and relative vorticity belong to the same tornado-scale  
220 vortex if they are within a distance of 1 km in the horizontal or vertical direction. We detect  
221 the tornado-scale vortices using the output at one-hour intervals from 26 h to 36 h.

222 There are 24 tornado-scale vortices identified in the 10-hour output (Table 1). In the  
223 table, the tornado-scale vortex is named with four digits. While the first two digits indicate  
224 the hours of the simulation, the last two digits is the series number at the same hour. There  
225 are four tornado-scale vortices with the maximum vertical motion more than  $30 \text{ m s}^{-1}$  and  
226 the maximum vertical component of relative vorticity larger than  $0.4 \text{ s}^{-1}$ . Except for the two  
227 tornado-scale vortices at 36 h, the others occur during 26 h-31 h with 10 cases at 27 h. The  
228 lull period is coincident with relatively weaker instantaneous maximum wind speed at 10  
229 m although there is little difference in the azimuthal mean maximum wind speed (Fig. 1).  
230 Examination indicates that the 10-m instantaneous wind speed maximum at 27 h is  
231 associated with M2701. It is suggested that the tornado-scale vortex can lead to the  
232 strongest wind gust in a TC.

233 Previous studies argued that the presence of the mesovortices intensifies the TC by  
234 mixing the high-entropy air in the eye into the eyewall (Persing and Montgomery 2003;  
235 Montgomery et al. 2006; Aberson et al. 2006). As shown in Figure 1, the azimuthal



236 maximum wind speed does not show any jump at 27 h, when there are 10 identified  
237 tornado-scale vortices. In the following discussion, we will show that the mixing indeed  
238 exits, but its effect on the azimuthal maximum wind speed cannot be detected. It is similar  
239 with the conclusion from idealized numerical experiments conducted by Bryan and  
240 Rotunno (2009). In fact, the azimuthal maximum wind speed ( $\sim 45 \text{ m s}^{-1}$ ) is rather steady  
241 during the 10-hour period after the innermost domain has been activated for two hours.

242 The number of the identified tornado-scale vortices is sensitive to the threshold of  
243 vertical motion. If we relax the threshold of maximum vertical motion to  $15 \text{ m s}^{-1}$ , we can  
244 identify 89 tornado-scale vortices during the 10-hour period (Fig. 4a). Nearly all the  
245 tornado-scale vortices still occur in the same semicircle of the enhanced eyewall  
246 reflectivity. The duration of the tornado-scale vortex is examined in the 3-second output.  
247 The duration is counted as the consecutive period during which the maximum vertical  
248 motion and relative vorticity are not less than the thresholds. For the thresholds of  $20 \text{ m s}^{-1}$   
249 in vertical motion and  $0.2 \text{ s}^{-1}$  in relative vorticity, the mean duration is 40 seconds and the  
250 longest is 138 seconds. We can conclude that the identified tornado-scale vortices are not  
251 repeatedly counted in the 1-hour output.

## 252 5. Spatial distribution of tornado-scale vortices

253 Figure 4a shows the location of the maximum vertical motions of the detected tornado-  
254 scale vortices. In this figure, we also plot the locations of the 89 tornado-scale vortices  
255 identified with the threshold of maximum vertical motion of  $15 \text{ m s}^{-1}$ . The tornado-scale  
256 vortices exclusively occur in the semicircle with intense convection from the east to the  
257 northwest (Fig. 2a). Nearly all of the identified cases occur in the inward side of the radius  
258 of maximum wind (RMW) or close to RMW, with two exceptions that are located outside



259 of the RMW (Fig. 4a). One is M2901, which is 11.8 km from the RMW, and the other is  
260 M3601 being 7.3 km from the RMW (Table 1). Close examination indicates that the two  
261 tornado-scale vortices occur between two high reflectivity bands.

262 Although the real tornado-scale vortices were observed by chance, they were also  
263 associated with the intense radar reflectivity within the hurricane eyewall and sharp  
264 horizontal reflectivity gradients (Aberson et al. 2006, Marks et al. 2008 and Aberson et al.  
265 2016). In agreement with these studies, all of the simulated tornado-scale vortices are  
266 associated with sharp horizontal reflectivity gradients and most of them occur in the inner  
267 edge of the intense eyewall convection within the RMW. As shown in Figure 2a, all of the  
268 10 cases at 27 h are located in the inner edge of the intense reflectivity. It is suggested that  
269 the tornado-scale vortex favorably occurs at the inner edge of the intense eyewall  
270 convection.

271 Using the smoothed fields, we also calculate the Richardson number for each tornado-  
272 scale (Table 1). It is calculated at each level and then averaged over a layer between 200  
273 m and 800 m within a radius of 1.5 km from the location of the maximum vertical motion.  
274 The Richardson number is small, and it is negative for seven cases. As suggested by Stern  
275 et al. (2016), the strong updraft is mainly within a kilometer of the surface and it is  
276 implausible for buoyancy to be the primary mechanism for vertical acceleration. In Figure  
277 4a, the Richardson number is also plotted, which is averaged over the 10-hour period. We  
278 can see that the tornado-scale vortices generally occur in the areas with the Richardson  
279 number less than 0.25. The areas coincide with the semicircle of the enhanced eyewall  
280 convection. Figure 4b further shows the field of the Richardson number at 27 h. The 10  
281 tornado-scale vortices are all in an environment with the Richardson number less than 0.1.



282 Since the Richardson number is calculated as the ratio of the moist static stability to the  
283 vertical wind shear in the TCBL, we speculate that the strong vertical wind shear in the  
284 inward side of the intense eyewall convection is an important factor for the development  
285 of tornado-scale vortices.

286 Figure 5 shows the vertical cross sections of tangential wind, radial wind, vertical  
287 motion, reflectivity and relative vorticity below 2.5 km, which are averaged in the northeast  
288 quadrant over the 10-hour period. Note that the radial locations of M2901 and M3601 are  
289 not shown in Figure 5 due to the effect of the limited innermost domain on the calculation  
290 of the azimuthal mean. Note that there are relatively small changes in the RMW during the  
291 10-hour period. The maximum vertical motions associated with the tornado-scale vortices  
292 are located inside the tilted RMW between the altitudes of 300 m and 1300 m. Most of  
293 them (71%) are found between 400 m and 600 m. The altitudes of the maximum vertical  
294 motions generally increase when the inflow layer deepens outward. Figures 5b and 5c  
295 further indicate that the tornado-scale vortices are generally found in the region of strong  
296 vertical motion averaged over the northeastern quadrant, where the vortices are detected,  
297 and large relative vorticity with sharp horizontal reflectivity gradient on the inward side of  
298 the eyewall.

## 299 **6. Tornado-scale vortex structure**

300 Using the high-resolution model output, we can explore the structural features of the  
301 simulated tornado-scale vortex. After examination of all of the identified 24 tornado-scale  
302 vortices, we find that they can be classified into three categories in structure.



303        The first category includes 17 cases, accounting for 71% of the total. Their structural  
304 features can be represented by M2701, one of the four strongest tornado-scale vortices,  
305 located 4.3 kilometers from the 500-m RMW inward (Table 1). In fact, the four strongest  
306 belong to the same category. In this category, nearly all of the maximum vertical motions  
307 occur around the altitude of 500 m, except M3001. The maximum vertical motion of  
308 M2701 is  $31.98 \text{ m s}^{-1}$  at the altitude of 400 m, while the maximum relative vorticity of  $0.55$   
309  $\text{s}^{-1}$  occurs at 200 m (Table 1). The 3D structure of the tornado-scale vortex can be clearly  
310 demonstrated by the streamlines of perturbation winds near the strong updraft (Fig. 6). The  
311 flows curl cyclonically upward from the surface (Fig. 6a). The tornado-scale vortex is  
312 manifested by a small-scale circulation extending upward to  $\sim 1.5$  km. Besides, the tornado-  
313 scale vortex is closely associated with horizontal rolls (Fig. 6b).

314        Figure 7 shows the vertical cross section of vertical motion, equivalent potential  
315 temperature, and simulated radar reflectivity along the line in Figure 3b for M2701. The  
316 inflow from the outward side and the outflow from the eye side converge near the surface  
317 to the strong updraft that is below  $\sim 1.5$  km. The updraft and the downward motion to its  
318 radially outward flank constitute a horizontal rolling vortex. On the top of the updraft, there  
319 is a layer of the high equivalent potential temperature ( $\theta_e$ ) layer (Fig. 7b). To the eye side  
320 of the updraft, there is a high  $\theta_e$  layer below  $\sim 1.5$  km. The high  $\theta_e$  layer tilts upward and  
321 extends outward. The large radar reflectivity can be found below the high  $\theta_e$  layer (Fig. 7c).  
322 The intense updraft is located in the inner edge of the large radar reflectivity region. While  
323 the large radar reflectivity is part of the eyewall, the high  $\theta_e$  layer should be the indication  
324 of the air in the eye. In addition, as suggested by Aberson et al. (2006) and Marks et al.



325 (2008), the strong updraft is within a saturated layer (Fig. 8a), coinciding with high relative  
326 vorticity (Fig. 8c).

327 To the right of the updraft (Fig. 7b), another high  $\theta_e$  layer can be seen at the altitude of  
328 ~500 m. We check other cases in the category and find that the lower-altitude high  $\theta_e$  layer  
329 does not always present. The downward motion at ~500 m may be responsible for the  
330 lower-altitude high  $\theta_e$  layer. The relatively low  $\theta_e$  near the surface corresponds to the inflow  
331 layer, which brings lower  $\theta_e$  into the updraft. The high  $\theta_e$  air meets with the cold inflow air,  
332 resulting in relatively lower  $\theta_e$  in the strong updraft. It is indicated that the high  $\theta_e$  air in  
333 the eye is entrained into the TC eyewall.

334 Previous studies have shown that the quasi-linear bands are closely associated with the  
335 horizontal rolls in the TC boundary due to the upward and downward momentum transports  
336 (Wurman and Winslow 1998; Katsaros et al. 2002; Morrison et al. 2005; Lorsolo et al.  
337 2008; Ellis and Businger 2010; Foster 2013). To demonstrate the relationship, Figure 8b  
338 shows the cross section of winds along the line shown in Figure 2b and the corresponding  
339 wind speeds at 10 m and 400 m. The figure clearly shows that the wind speed fluctuations  
340 at 10 m are associated with the changes of the vertical motions. The wind speed jump is  
341 significant across the intense updraft (Fig. 8b). At 10 m, the wind speed suddenly increases  
342 from ~30 m s<sup>-1</sup> to ~65 m s<sup>-1</sup>. Note that the wind speed jump is larger at 400 m, ranging from  
343 ~35 m s<sup>-1</sup> to ~90 m s<sup>-1</sup>. Marks et al. (2008) reported that the wind speed at 450-m altitude  
344 increased rapidly from <40 m s<sup>-1</sup> to 89 m s<sup>-1</sup> in the Hurricane Hugo (1989) when the NOAA  
345 research aircraft encountered an EVM. While the downward motion is consistent with the  
346 strong wind speed jumps, we argue that the superposition of the cyclonic circulation of the



347 tornado-scale vortex also play an important role in enhancing wind gusts on its radially  
348 outward side.

349 There are three tornado-scale vortices in the second category, including M2706, M2707  
350 and M2708. The structural features can be represented by M2708. In M2708, the maximum  
351 vertical motion and relative vorticity occur at 900 m and 800 m, respectively (Table 1).  
352 The vertical motion of more than  $12 \text{ m s}^{-1}$  extends vertically from the near surface to  $\sim 2$   
353 km (Fig. 9a). In this category, we cannot see the warm air with high  $\theta_e$  (Fig. 9b) and the  
354 strong updraft is located in a statically unstable stratification (Table 1). The wind speed at  
355 the altitude of 900 m varies by  $\sim 20 \text{ m s}^{-1}$  across the updraft, while the wind speed gradient  
356 is relatively weak at 10 m (Fig. 9c).

357 The third category includes four cases: M2600, M2703, M2705 and M3002, in which  
358 the updraft occurs in a statically stable stratification (Table 1). Here we use M3002 as an  
359 example to show its vertical structure. As shown in Figures 10a, the updraft is elevated  
360 between 0.5 km and 2 km. The maximum vertical motion and relative vorticity are found  
361 at the altitude of 1300 m. In this category, a pronounced feature is the deep low  $\theta_e$  (less  
362 than 364 K) layer in the inflow layer (Fig. 10b). As shown in Figure 10c, the gradient of  
363 the wind speed at 10 m is not clear while there is a speed jump of  $\sim 30 \text{ m s}^{-1}$  in the vicinity  
364 of the updraft at 1300 m.

## 365 7. Summary

366 The tornado-scale vortex or EVM in the TCBL has been observed in intense hurricanes  
367 and is always associated strong turbulence. To understand complicated interactions of the  
368 large-scale background flow, TC vortex, mesoscale organization, down to fine-scale





369 turbulent eddies, a numerical experiment in which a TC evolves in a typical large-scale  
370 background over the western North Pacific is conducted using the WRF-LES framework  
371 with six nesting grids. The simulated tornado-scale vortex shows the similar features as  
372 revealed with the limited observational data, including the updraft/downdraft couplet, the  
373 sudden jump of the wind speed, the favorable location, and the horizontal scale. It is  
374 suggested that the WRF-LES framework can successfully simulate the tornado-scale  
375 vortex with the grids at the resolution of 37 m that cover the TC eye and eyewall.

376 Following Wu et al. (2018), the tornado-scale vortex can be defined as a small-scale  
377 cyclonic circulation with the maximum vertical motion not less than  $20 \text{ m s}^{-1}$  and maximum  
378 relative vorticity not less than  $0.2 \text{ s}^{-1}$ . A total of 24 tornado-scale vortices can be identified  
379 in the 10-hour output. Nearly all of them are within or close to the RMW. Most of them  
380 occur in the inward side of the intense eyewall convection, mostly below the altitude of 2  
381 km. Tornado-scale vortices are mostly in neutral or stable stratification within the saturated,  
382 high- $\theta_e$  layer. The tornado-scale vortex generally occurs in the areas with the Richardson  
383 number less than 0.25. We speculate that the strong vertical wind shear in the inward side  
384 of the intense eyewall convection is an important factor for the development of tornado-  
385 scale vortices.

386 The simulated tornado-scale vortex has a small horizontal scale of 1-2 km in the TCBL.  
387 It is accompanied by strong updrafts (more than  $15 \text{ m s}^{-1}$ ) and a cyclonic circulation with  
388 large vertical components of relative vorticity (larger than  $0.2 \text{ s}^{-1}$ ). The tornado-scale vortex  
389 is closely associated with horizontal rolls. Nearly in all of the simulated tornado-scale  
390 vortex cases, the narrow intense updraft is coupled with the relatively broad downdraft,  
391 constituting an updraft/downdraft couplet or horizontal rolling vortex, as observed by the



392 research aircraft. Since the tornado-scale vortex is associated with intense updrafts and  
393 strong wind gusts, its presence can pose a severe threat to the eyewall penetration of  
394 manned research aircraft and the strong wind gusts associated with tornado-scale vortices  
395 can pose a severe risk to coastal life and property.

396 **Acknowledgments.** We thank Prof. Ping Zhu of Florida International University for aiding  
397 with the WRF-LES framework. This research was jointly supported by the National Basic  
398 Research Program of China (2015CB452803), the National Natural Science Foundation of  
399 China (41730961, 41675051, 41675009), and Jiangsu Provincial Natural Science Fund  
400 Project (BK20150910). The numerical simulation was carried out on the Tianhe  
401 Supercomputer, China.

## 402 **References**

- 403 Aberson, S. D., Black, M., Montgomery, M. T. and Bell, M.: Hurricane Isabel (2003):  
404 New Insights Into the Physics of Intense Storms. Part II: Extreme Localized  
405 Wind, *Bull. Amer. Meteor. Soc.*, **87**, 2006.
- 406 Aberson, S. D., Zhang, J. A. and Ocasio, K. N.: An Extreme Event in the Eyewall of  
407 Hurricane Felix on 2 September 2007, *Mon. Wea. Rev.*, **145**, 2017.
- 408 Braun, S. A. and Tao, W.-K.: Sensitivity of High-Resolution Simulations of Hurricane  
409 Bob (1991) to Planetary Boundary Layer Parameterizations. *Monthly Weather*  
410 *Review*, **128**, 3941–3961, 2000.
- 411 Braun, S. A. and Wu, L.: A Numerical Study of Hurricane Erin (2001). Part II: Shear and  
412 the Organization of Eyewall Vertical Motion. *Monthly Weather Review*, **135**,  
413 1179–1194, 2007.



- 414 Bryan, G. H., and R. Rotunno: The influence of near-surface, high-entropy air in  
415 hurricane eyes on maximum hurricane intensity. *J. Atmos. Sci.*, **66**, 148–158,  
416 2009.
- 417 Bryan, G. H.: Effects of surface exchange coefficients and turbulence length scales on the  
418 intensity and structure of numerically simulated hurricanes. *Mon. Wea. Rev.*, **140**,  
419 1125–1143, 2012.
- 420 Bryan, G. H., Stern, D. P., and Rotunno, R.: A Framework for Studying the Inner Core of  
421 Tropical Cyclones Using Large Eddy Simulation, paper presented at 31st  
422 Conference on Hurricanes and Tropical Meteorology, *Am. Meteorol. Soc.*, San  
423 Diego, Calif, 2014.
- 424 Duchon, C. E.: Lanczos filtering in one and two dimensions. *J. Appl. Meteor.*, **18**, 1016–  
425 1022, 1979.
- 426 Dudhia, J.: Numerical study of convection observed during the winter monsoon  
427 experiment using a mesoscale two-dimensional model. *J. Atmos. Sci.*, **46**, 3077–  
428 3107, 1989.
- 429 Ellis, R. and Businger, S.: Helical Circulations in the Typhoon Boundary Layer. *Journal*  
430 *of Geophysical Research*, **115**, D06205, 2010.
- 431 Foster, R.: Why rolls are prevalent in the hurricane boundary layer. *Journal of the*  
432 *atmospheric sciences*, **62**, 2647–2661, 2005.
- 433 Foster, R.: Signature of Large Aspect Ratio Roll Vortices in Synthetic Aperture Radar  
434 Images of Tropical Cyclones. *Oceanography*, **26**, 58-67, 2013.
- 435 Frank, W. M. and Ritchie, E. A.: Effects of vertical wind shear on the intensity and  
436 structure of numerically simulated hurricanes. *Mon. Wea. Rev.*, **129**, 2249-2269,  
437 2001.
- 438 Gao, K. and Ginis, I.: On the Generation of Roll Vortices due to the Inflection Point  
439 Instability of the Hurricane Boundary Layer Flow. *Journal of the Atmospheric*  
440 *Sciences*, **71**, 4292–4307, 2014.



- 441 Gao, K., Ginis, I., Doyle, J. D. and Jin, Y.: Effect of Boundary Layer Roll Vortices on the  
442 Development of an Axisymmetric Tropical Cyclone. *Journal of the Atmospheric*  
443 *Sciences*, **74**, 2737–2759, 2017.
- 444 Green, B. W. and Zhang, F.: Sensitivity of Tropical Cyclone Simulations to Parametric  
445 Uncertainties in Air–Sea Fluxes and Implications for Parameter Estimation.  
446 *Monthly Weather Review*, **142**, 2290–2308, 2014.
- 447 Green, B. W. and Zhang, F.: Numerical simulations of Hurricane Katrina (2005) in the  
448 turbulent gray zone, *Journal of Advances in Modeling Earth Systems*, **7**, 142–161,  
449 2015.
- 450 Hong, S.–Y. and Lim, J.–O. J.: The WRF single–moment 6–class microphysics scheme  
451 (WSM6). *J. Korean Meteor. Soc.*, **42**, 129–151, 2006.
- 452 Kain, J. S. and Fritsch, J. M.: Convective parameterization for mesoscale models: The  
453 Kain–Fritsch scheme. *The Representation of Cumulus Convection in Numerical*  
454 *Models*, Meteor. Monogr., Amer. Meteor. Soc., **46**, 165–170, 1993.
- 455 Kosiba, K., Wurman, J., Masters, F. J., and Robinson, P.: Mapping of Near-Surface  
456 Winds in Hurricane Rita Using Finescale Radar, Anemometer, and Land-Use  
457 Data. *Monthly Weather Review*, **141**, 4337–4349, 2013.
- 458 Kosiba, K. A. and Wurman, J.: Finescale Dual-Doppler Analysis of Hurricane Boundary  
459 Layer Structures in Hurricane Frances (2004) at Landfall. *Monthly Weather*  
460 *Review*, **142**, 1874–1891, 2014.
- 461 Lorsolo, S., Schroeder, J. L., Dodge, P., and Marks, F.: An Observational Study of  
462 Hurricane Boundary Layer Small-Scale Coherent Structures. *Monthly Weather*  
463 *Review*, **136**, 2871–2893, 2008.
- 464 Marks, F. D., Black, P. G., Montgomery, M. T., and Burpee, R. W.: Structure of the Eye  
465 and Eyewall of Hurricane Hugo (1989). *Monthly Weather Review*, **136**, 1237–  
466 1259, 2008.



- 467 Mirocha, J. D., Lundquist, J. K., and Kosović, B.: Implementation of a Nonlinear  
468 Subfilter Turbulence Stress Model for Large-Eddy Simulation in the Advanced  
469 Research WRF Model. *Monthly Weather Review*, **138**, 4212–4228, 2010.
- 470 Mlawer, E. J., Taubman, S. J., Brown, P. D., Iacono, M. J., and Clough, S. A.: Radiative  
471 transfer for inhomogeneous atmosphere: RRTM, a validated correlated-k model  
472 for the longwave. *J. Geophys. Res.*, **102 (D14)**, 16663–16682, 1997.
- 473 Montgomery, M. T., Bell, M. M., Aberson, S. D., and Black, M. L.: Hurricane Isabel  
474 (2003): New Insights into the Physics of Intense Storms. Part I: Mean Vortex  
475 Structure and Maximum Intensity Estimates. *Bull. Amer. Meteor. Soc.*, **87**, 1335–  
476 1347, 2006.
- 477 Morrison, I., Businger, S., Marks, F., Dodge, P., and Businger, J. A.: An Observational  
478 Case for the Prevalence of Roll Vortices in the Hurricane Boundary Layer.  
479 *Journal of the atmospheric sciences*, **62**, 2662–2673, 2005.
- 480 Noh, Y., Cheon, W. G., Hong, S.-Y. and Raasch, S.: Improvement of the K-profile model  
481 for the planetary boundary layer based on large-eddy simulation data. *Bound.-*  
482 *Layer Meteor.*, **107**, 401–427, 2003.
- 483 Persing, J. and Montgomery, M. T.: Hurricane Superintensity. *J. Atmos. Sci.*, **60**, 2349–  
484 2371, 2003.
- 485 Pielke, R. A., Gratz, J., Landsea, C. W., Collins, D., Saunders, M. A., and Musulin, R.:  
486 Normalized Hurricane Damage in the United States: 1900–2005. *Natural Hazards*  
487 *Review*, **9**, 29–42, 2008.
- 488 Rotunno, R., Chen, Y., Wang, W., Davis, C., Dudhia, J., and Holland, G. J.: Large-Eddy  
489 Simulation of an Idealized Tropical Cyclone. *Bulletin of the American*  
490 *Meteorological Society*, **90**, 1783–1788, 2009.
- 491 Rotunno, R. and Bryan, G. H.: Effects of resolved turbulence in a large eddy simulation  
492 of a hurricane, paper presented at 31st Conference on Hurricanes and Tropical  
493 Meteorology, *Am. Meteorol. Soc.*, San Diego, Calif, 2014.



- 494 Smith, R. K. and Montgomery, M. T.: Hurricane boundary-layer theory. *Quarterly*  
495 *Journal of the Royal Meteorological Society*, **136**, 1665–1670, 2010.
- 496 Stern, D. P. and Bryan, G. H.: The structure and dynamics of coherent vortices in the  
497 eyewall boundary layer of tropical cyclones, paper presented at 31st Conference  
498 on Hurricanes and Tropical Meteorology, *Am. Meteorol. Soc.*, San Diego, Calif,  
499 2014.
- 500 Wakimoto, R. M. and Black, P. G.: Damage Survey of Hurricane Andrew and Its  
501 Relationship to the Eyewall. *Bull. Amer. Meteor. Soc.*, **75**, 189–200, 1994.
- 502 Wurman, J. and Winslow, J.: Intense Sub-Kilometer-Scale Boundary Layer Rolls  
503 Observed in Hurricane Fran. *Science*, **280**, 555–557, 1998.
- 504 Wurman, J. and Kosiba, K.: The Role of Small-Scale vortices in Enhancing Surface  
505 Winds and Damage in Hurricane Harvey (2017). *Mon. Wea. Rev.*, **146**, 713-722,  
506 2018.
- 507 Wu, L., Liu, Q., and Li, Y.: Prevalence of tornado-scale vortices in the tropical cyclone  
508 eyewall. *Proceedings of the National Academy of Sciences*,  
509 [doi.org/10.1073/pnas.1807217115](https://doi.org/10.1073/pnas.1807217115), 2018.
- 510 Wu, L., Braun, S. A., Halverson, J., and Heymsfield, G.: A numerical study of Hurricane  
511 Erin (2001). Part I: Model verification and storm evolution. *J. Atmos. Sci.*, **63**, 65–  
512 86, 2006.
- 513 Wu, L. and Chen, X.: Revisiting the steering principle of tropical cyclone motion in a  
514 numerical experiment. *Atmos. Chem. Phys.*, **16**, 14925–14936, 2016.
- 515 Zhang, Q., Wu, L., and Liu, Q.: Tropical Cyclone Damages in China 1983–2006. *Bull.*  
516 *Amer. Meteor. Soc.*, **90**, 489–495, 2009.
- 517 Zhu, P.: Simulation and Parameterization of the Turbulent Transport in the Hurricane  
518 Boundary Layer by Large Eddies. *Journal of Geophysical Research*, **113**,  
519 D17104, 2008.



520 Zhu, P., Menelaou, K. and Zhu, Z.: Impact of Subgrid-Scale Vertical Turbulent Mixing  
521 on Eyewall Asymmetric Structures and Mesovortices of Hurricanes: Impact of  
522 SGS Vertical Turbulent Mixing on Eyewall Asymmetries. *Quarterly Journal of*  
523 *the Royal Meteorological Society*, **140**, 416–438, 2013.

524

525

526

527



528

529 **Table caption**

530 Table 1 List of the identified tornado-scale vortices in the TCBL with the maximum  
531 updraft ( $\text{m s}^{-1}$ ) and relative vorticity ( $\text{s}^{-1}$ ) and the corresponding altitudes (m) in  
532 the parentheses. The location column lists the radial distance from the TC center  
533 and the relative distance to the 500-m radius of maximum wind in the parentheses.  
534 The Richardson number (Ri) is averaged over the layer between 200-800 m  
535 within a radius of 1.5 km. The four strongest EVMs are indicated in bold.

536

537





538 **Figure caption**

539 Figure 1 Intensity of the simulated tropical cyclone during 24–36 h in terms of  
540 instantaneous (red) and azimuthal (blue) maximum wind speeds at 10 m.

541 Figure 2 Simulated radar reflectivity (dBZ) at 500 m (a) and wind speed ( $\text{m s}^{-1}$ ) at 10  
542 m (b) within an area of  $40 \times 40 \text{ km}^2$  at 27 h. The plus signs and solid circles  
543 indicate the TC center and the radius of maximum wind. The rectangle shows  
544 the area used in Fig. 3a. The arrow shows the vertical wind shear of  $7.0 \text{ (27h)}$   
545  $\text{m s}^{-1}$  between 200 hPa and 850 hPa.

546 Figure 3 (a) 10-m wind speed ( $\text{m s}^{-1}$ ) and wind vectors and (b) the perturbation wind  
547 vectors and vertical component of relative vorticity (shading) at 500 m in the  
548 area shown in Fig. 2b. The straight line is the location of the vertical cross  
549 section in Figure 7 and M2701 and M2705 are the two tornado-scale vortices in  
550 the small area.

551 Figure 4 (a) Horizontal distribution of the tornado-scale vortices identified with the  
552 thresholds of  $15 \text{ m s}^{-1}$  (yellow dots) and  $20 \text{ m s}^{-1}$  (red dots) in vertical motion  
553 and the Richardson number (shading) averaged over 26–36 h; (b) the same as  
554 (a), but for 27 h. The solid circle is the 500-km radius of maximum wind and  
555 dashed circles indicate the distances from the TC center at 10-km intervals.

556 Figure 5 Vertical cross sections of (a) tangential (shading) and radial (contour,  
557 interval:  $2 \text{ m s}^{-1}$ ) wind speeds, (b) upward motion (contour, interval:  $0.5 \text{ m s}^{-1}$ )  
558 and radar reflectivity (shading), and (c) tangential wind (contour, interval:  $4 \text{ m s}^{-1}$ )  
559 and the vertical component of relative vorticity (shading, unit:  $\text{s}^{-1}$ ), which are  
560 averaged over the northeastern quadrant during 26 h–36 h. The dots are the  
561 locations of identified tornado-scale vortices. The dashed white lines indicate  
562 the radius of maximum wind. The vertical and horizontal axes indicate the  
563 altitude (km) from the surface and the relative distances (km) from the TC  
564 center.



565 Figure 6 (a) The streamlines of the horizontal perturbation winds for M2701 and the  
566 wind speed (shading) at the altitude of 10 m. (b) The vertical slice of the  
567 perturbation winds for M2701. The warm (cold) color of the streamline  
568 indicates the upward (downward) vertical velocity perturbation and the vectors  
569 show the near-surface wind fields. The vertical and horizontal axes indicate the  
570 altitude (km) from the surface and the relative distances (km) from the nearest  
571 corner, respectively.

572 Figure 7 The vertical cross sections of the perturbation winds (vector) and (a)  
573 vertical motion, (b) equivalent potential temperature, and (c) radar reflectivity  
574 (shading) for M2701 along the line in Figure 3b. The abscissa indicates the  
575 relative outward distance.

576 Figure 8 (a) the vertical cross section of perturbation winds (vector) and relative  
577 humidity (shading) for M2701, (b) the 500-m (blue) and 10-m (black) wind  
578 speeds and the 400-m relative vorticity for M2701 along the line in Figure 3b.  
579 The abscissa indicates the relative outward distance.

580 Figure 9 The vertical cross sections of the perturbation winds (vector) and (a)  
581 vertical motion, (b) equivalent potential temperature for M2708, and (c) the  
582 corresponding 900-m (blue) and 10-m (black) wind speeds. The abscissa  
583 indicates the relative outward distance.

584 Figure 10 The vertical cross sections of the perturbation winds (vector) and (a)  
585 vertical motion, (b) equivalent potential temperature for M3002, and (c) the  
586 corresponding 1300-m (blue) and 10-m (black) wind speeds. The abscissa  
587 indicates the relative outward distance. The abscissa indicates the relative  
588 outward distance.

589

590

591

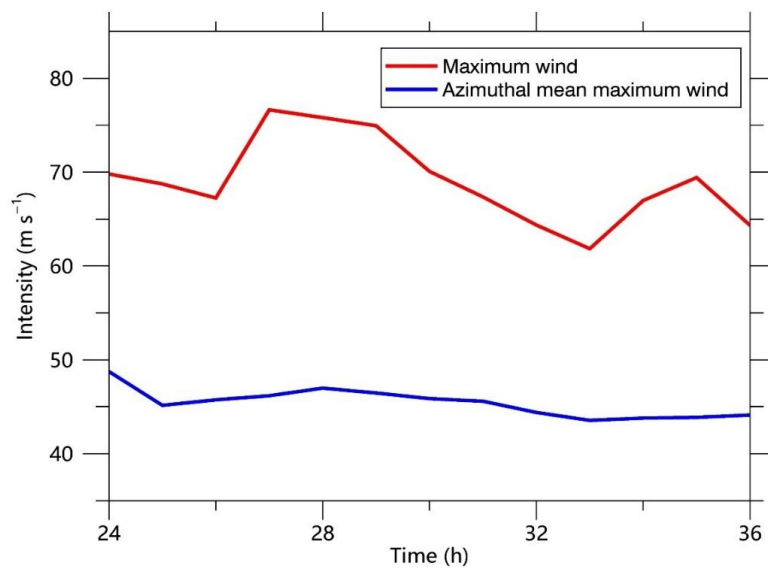


592 Table 1 List of the identified tornado-scale vortices in the TCBL with the maximum updraft  
 593 ( $\text{m s}^{-1}$ ) and relative vorticity ( $\text{s}^{-1}$ ) and the corresponding altitudes (m) in the parentheses.  
 594 The location column lists the radial distance from the TC center and the relative distance  
 595 to the 500-m radius of maximum wind in the parentheses. The Richardson number (Ri) is  
 596 averaged over the layer between 200-800 m **within** a radius of 1.5 km. The four strongest  
 597 EVMs are indicated in bold.

No.	Updraft	Vorticity	Location	Ri
M2600	22.75(800)	0.36(400)	23.6 (-5.5)	0.095
M2601	22.39(600)	0.23(500)	25.3 (-3.8)	0.111
M2700	27.37(500)	0.45(200)	25.6 (-3.0)	0.017
<b>M2701</b>	<b>31.98(400)</b>	<b>0.55(200)</b>	<b>24.3 (-4.3)</b>	<b>-0.008</b>
M2702	21.40(300)	0.30(300)	21.1 (-7.5)	0.029
M2703	20.46(400)	0.23(400)	27.9 (-0.7)	0.013
M2704	27.76(500)	0.34(400)	22.8 (-5.8)	0.032
M2705	22.26(600)	0.24(600)	27.9 (-0.7)	0.038
M2706	20.93(600)	0.23(500)	20.7 (-7.9)	-0.031
M2707	20.30(700)	0.21(700)	29.6 (1.0)	-0.011
M2708	22.20(900)	0.29(800)	31.2 (2.6)	-0.037
M2709	21.49(800)	0.22(800)	22.8 (-5.8)	0.052
M2800	20.12(400)	0.23(400)	27.0 (-1.7)	0.030
M2801	24.36(600)	0.39(400)	24.2 (-4.5)	-0.037
M2802	22.14(600)	0.30(500)	29.0 (0.3)	0.029
M2803	20.14(500)	0.23(500)	26.6 (-2.1)	0.025
<b>M2900</b>	<b>34.98(400)</b>	<b>0.48(200)</b>	<b>27.5 (-1.7)</b>	<b>0.042</b>
M2901	20.95(400)	0.21(400)	41.0 (11.8)	0.017
<b>M3000</b>	<b>35.77(400)</b>	<b>0.48(300)</b>	<b>28.1 (-0.1)</b>	<b>0.044</b>
<b>M3001</b>	<b>38.33(900)</b>	<b>0.49(400)</b>	<b>27.7 (-0.5)</b>	<b>0.067</b>
M3002	21.43(1300)	0.29(1300)	29.8 (1.6)	0.083
M3100	20.87(600)	0.24(700)	25.1 (-3.3)	-0.106
M3600	22.00(400)	0.35(400)	24.1 (-6.6)	0.146
M3601	22.68(600)	0.23(500)	38.0 (7.3)	-0.073



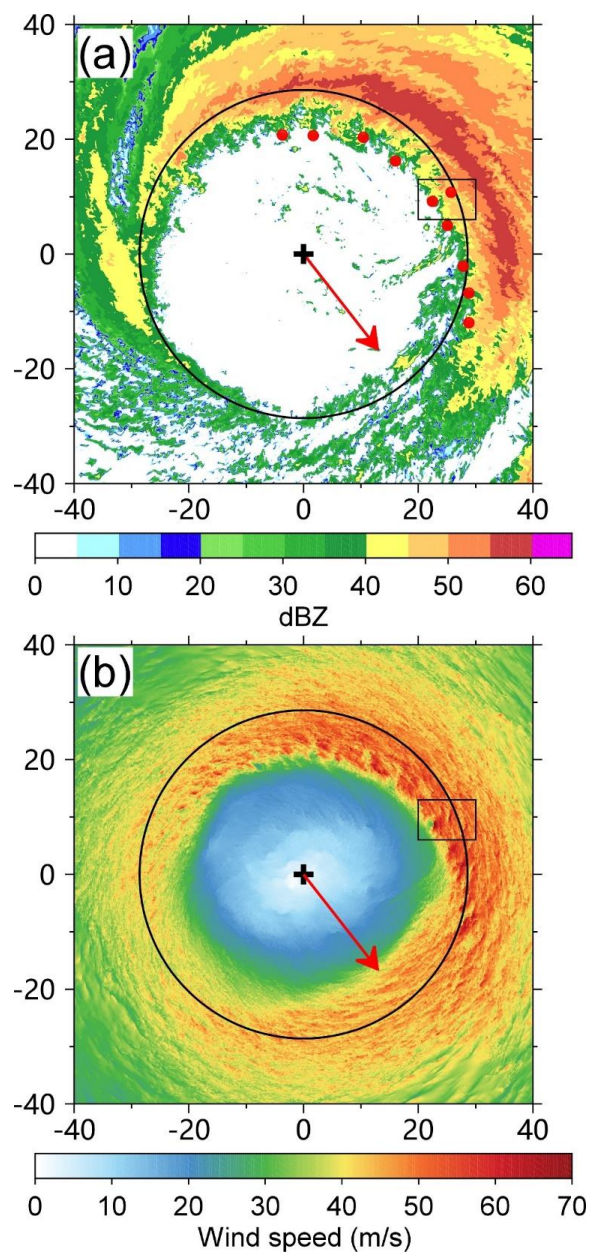
598



599

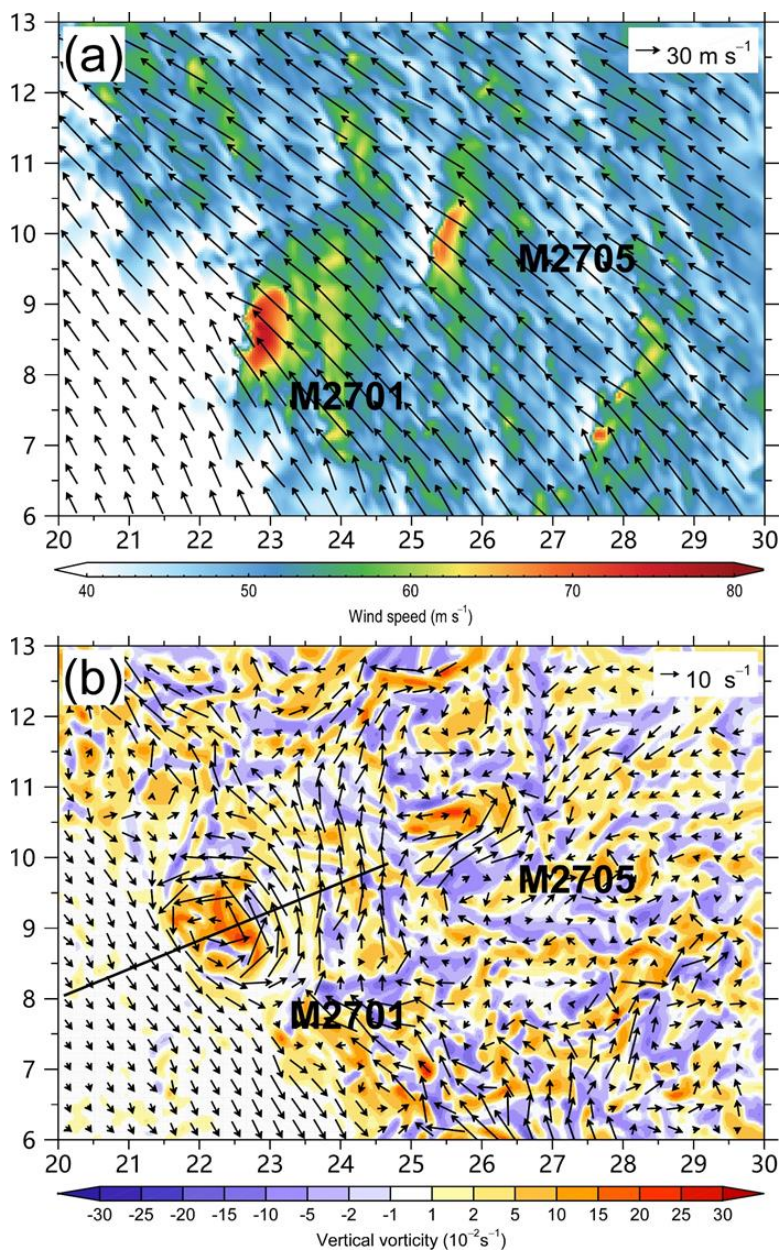
600 Figure 1 Intensity of the simulated tropical cyclone during 24-36 h in terms of  
601 instantaneous (red) and azimuthal (blue) maximum wind speeds at 10 m.

602



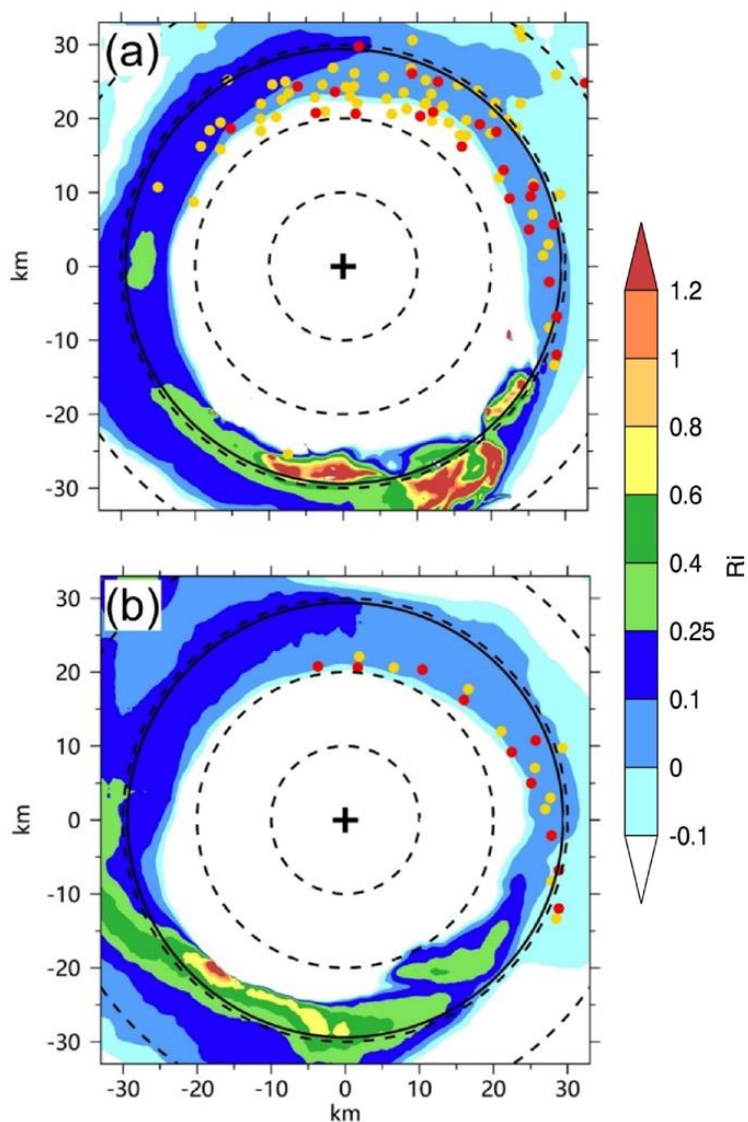
603

604 Figure 2 Simulated radar reflectivity (dBZ) at 500 m (a) and wind speed ( $\text{m s}^{-1}$ ) at 10 m (b)  
 605 within an area of  $40 \times 40 \text{ km}^2$  at 27 h. The plus signs and solid circles indicate the TC center  
 606 and the radius of maximum wind. The rectangle shows the area used in Fig. 3a. The arrow  
 607 shows the vertical wind shear of  $7.0 (27\text{h}) \text{ m s}^{-1}$  between 200 hPa and 850 hPa.



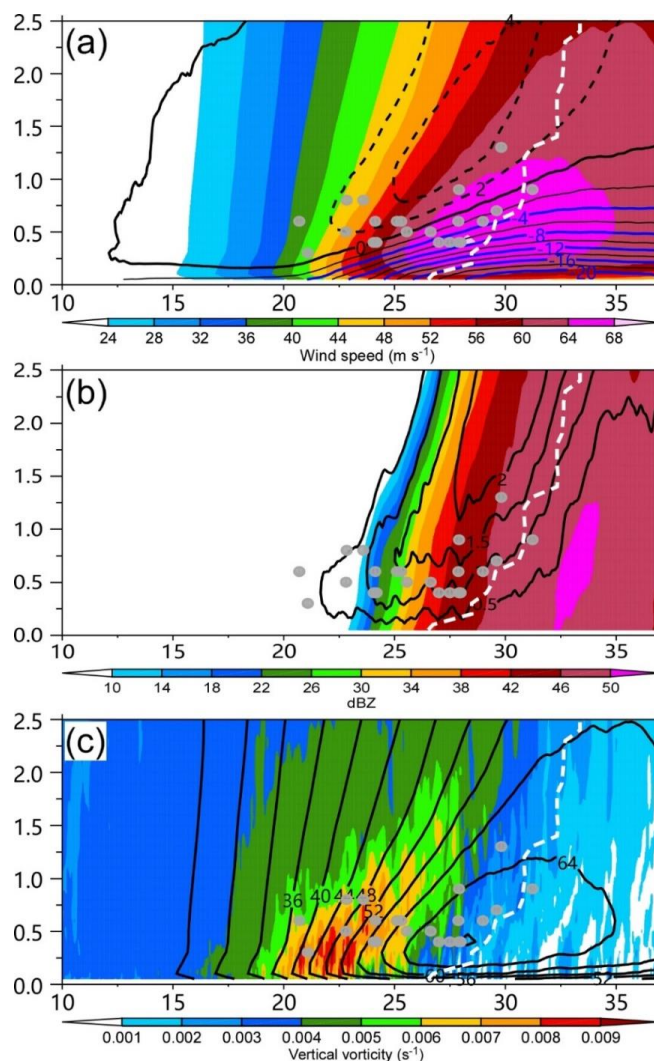
608

609 Figure 3 (a) 10-m wind speed ( $\text{m s}^{-1}$ ) and wind vectors and (b) the perturbation wind vectors  
610 and vertical component of relative vorticity (shading) at 500 m in the area shown in Fig.  
611 2b. The straight line is the location of the vertical cross section in Figure 7 and M2701 and  
612 M2705 are the two tornado-scale vortices in the small area.



613

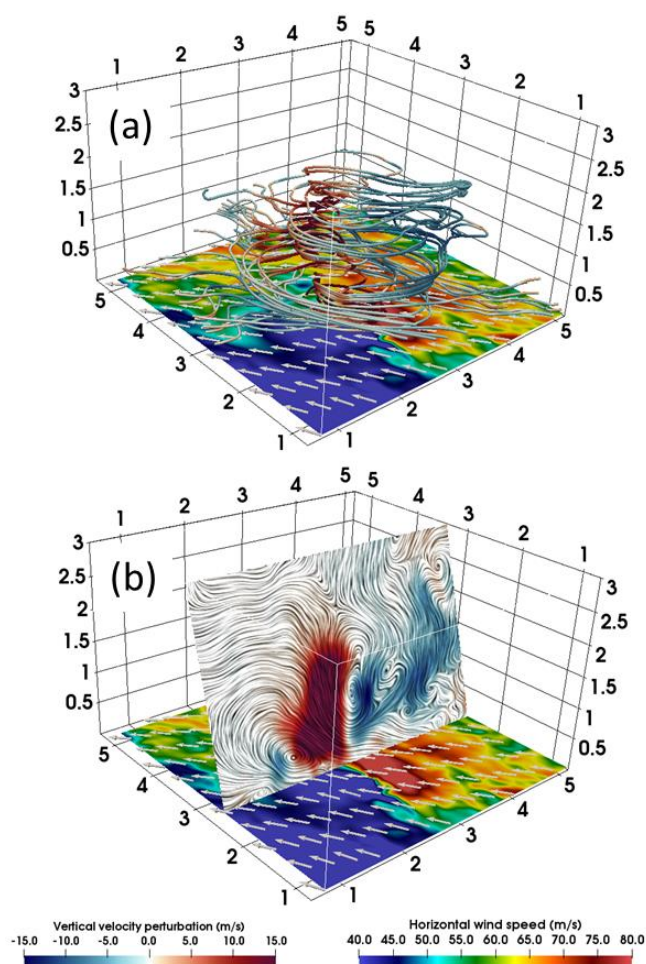
614 Figure 4 (a) Horizontal distribution of the tornado-scale vortices identified with the  
615 thresholds of  $15 \text{ m s}^{-1}$  (yellow dots) and  $20 \text{ m s}^{-1}$  (red dots) in vertical motion and the  
616 Richardson number (shading) averaged over 26–36 h; (b) the same as (a), but for 27 h. The  
617 solid circle is the 500-km radius of maximum wind and dashed circles indicate the  
618 distances from the TC center at 10-km intervals.



619

620 Figure 5 Vertical cross sections of (a) tangential (shading) and radial (contour, interval: 2  
621 m s<sup>-1</sup>) wind speeds, (b) upward motion (contour, interval: 0.5 m s<sup>-1</sup>) and radar reflectivity  
622 (shading), and (c) tangential wind (contour, interval: 4 m s<sup>-1</sup>) and the vertical component of  
623 relative vorticity (shading, unit: s<sup>-1</sup>), which are averaged over the northeastern quadrant  
624 during 26 h-36 h. The dots are the locations of identified tornado-scale vortices. The dashed  
625 white lines indicate the radius of maximum wind. The vertical and horizontal axes indicate  
626 the altitude (km) from the surface and the relative distances (km) from the TC center.





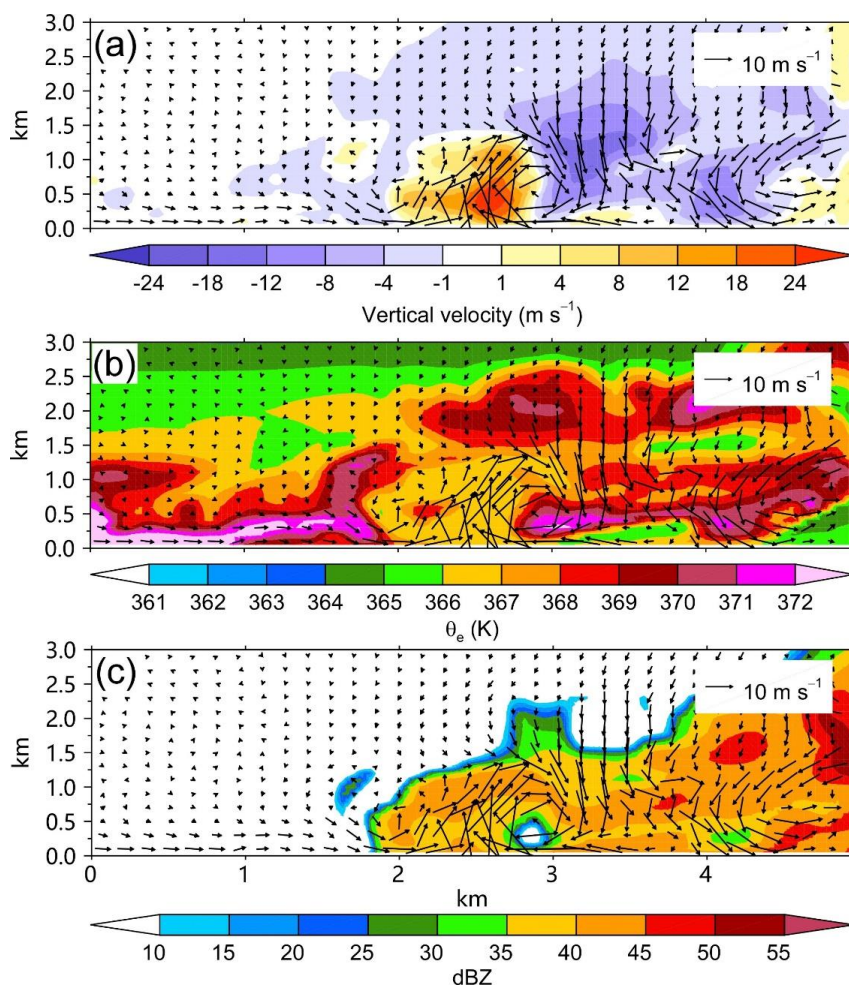
627

628 Figure 6 (a) The streamlines of the horizontal perturbation winds for M2701 and the wind  
 629 speed (shading) at the altitude of 10 m. (b) The vertical slice of the perturbation winds for  
 630 M2701. The warm (cold) color of the streamline indicates the upward (downward) vertical  
 631 velocity perturbation and the vectors show the near-surface wind fields. The vertical and  
 632 horizontal axes indicate the altitude (km) from the surface and the relative distances (km)  
 633 from the nearest corner, respectively.

634

635

636

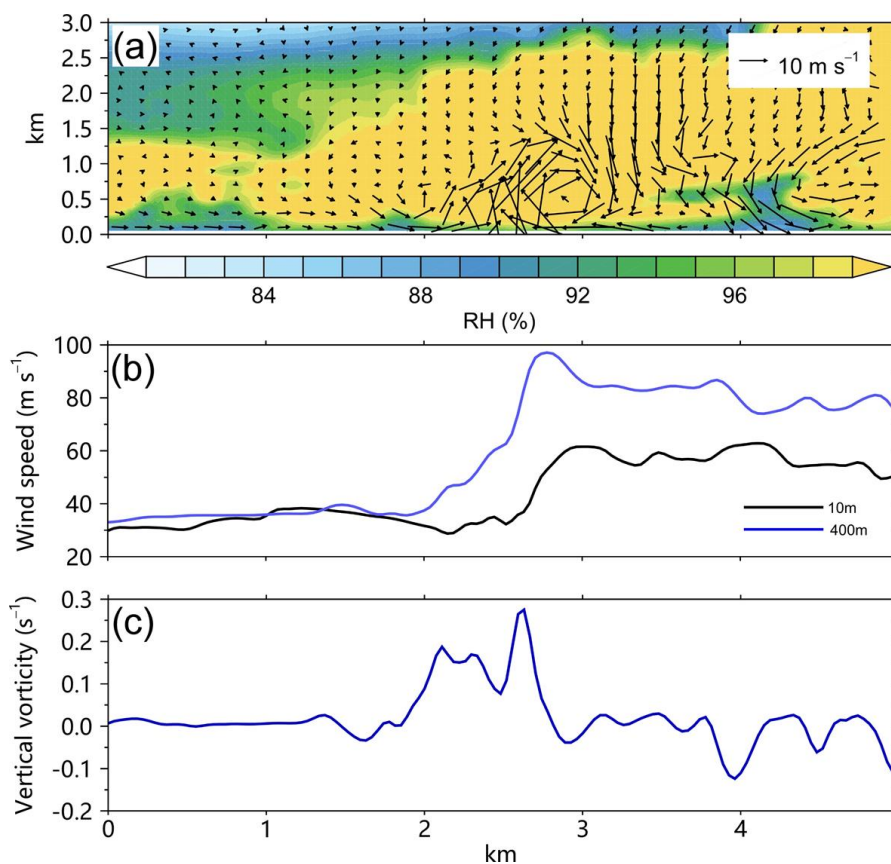


637

638 Figure 7 The vertical cross sections of the perturbation winds (vector) and (a) vertical  
639 motion, (b) equivalent potential temperature, and (c) radar reflectivity (shading) for M2701  
640 along the line in Figure 3b. The abscissa indicates the relative outward distance.

641

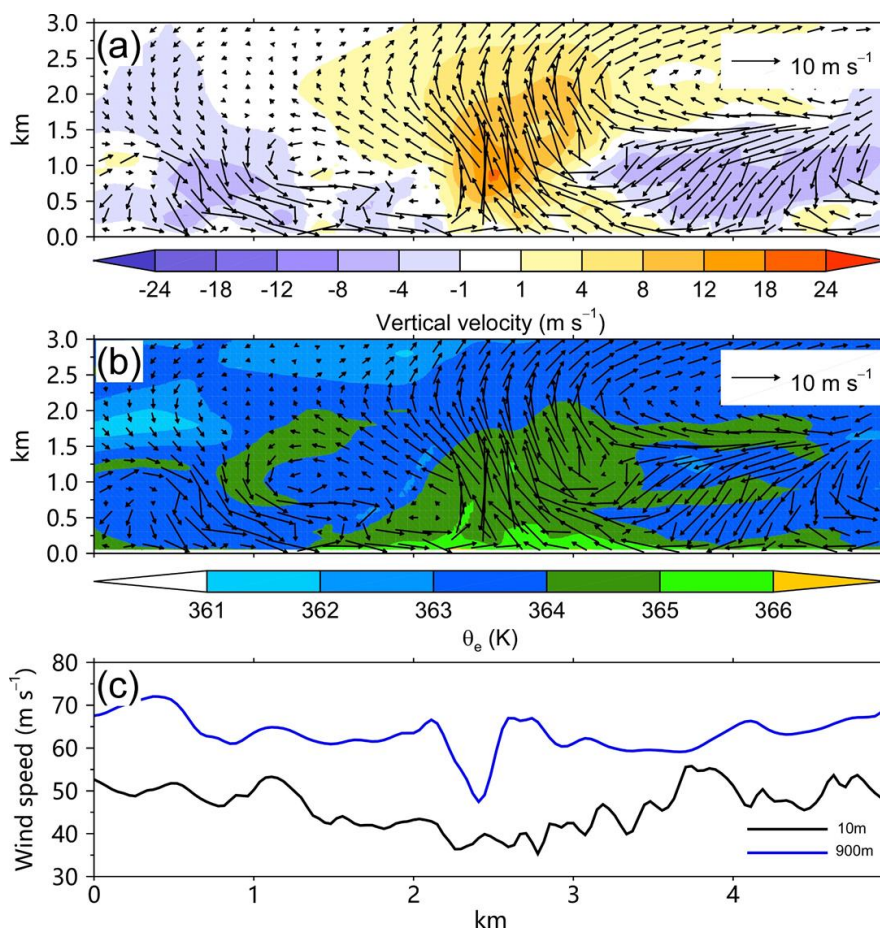
642



643

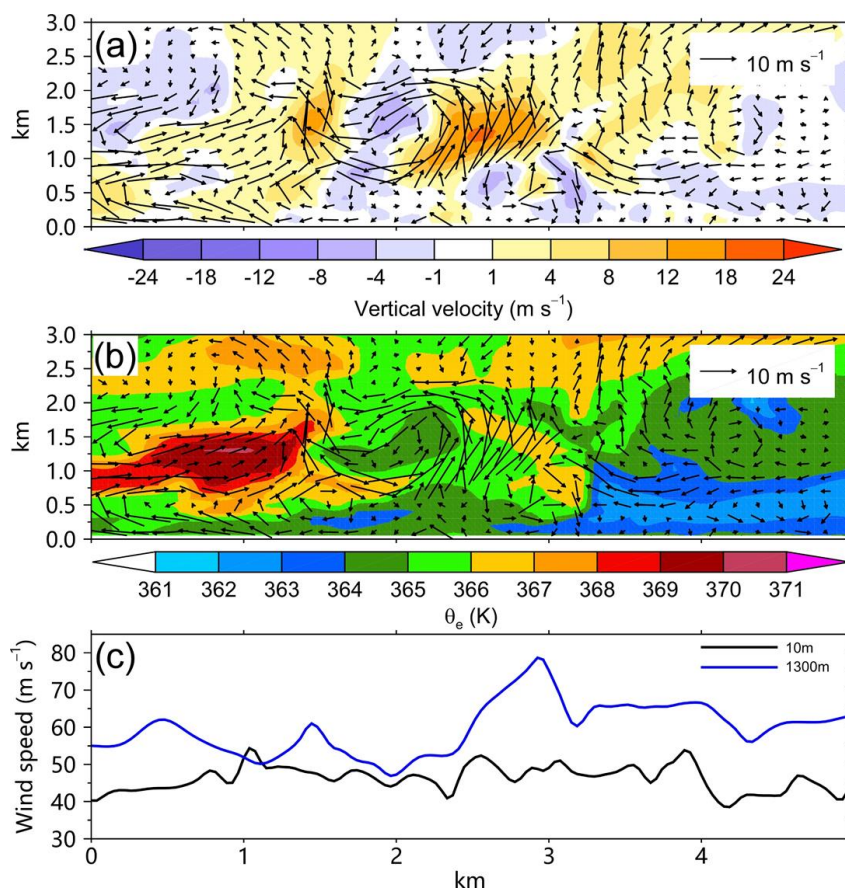
644 Figure 8 (a) the vertical cross section of perturbation winds (vector) and relative humidity  
 645 (shading) for M2701, (b) the 500-m (blue) and 10-m (black) wind speeds and the 400-m  
 646 relative vorticity for M2701 along the line in Figure 3b. The abscissa indicates the relative  
 647 outward distance.

648



649

650 Figure 9 The vertical cross sections of the perturbation winds (vector) and (a) vertical  
651 motion, (b) equivalent potential temperature for M2708, and (c) the corresponding 900-m  
652 (blue) and 10-m (black) wind speeds. The abscissa indicates the relative outward distance.



653

654 Figure 10 The vertical cross sections of the perturbation winds (vector) and (a) vertical  
 655 motion, (b) equivalent potential temperature for M3002, and (c) the corresponding 1300-  
 656 m (blue) and 10-m (black) wind speeds. The abscissa indicates the relative outward  
 657 distance. The abscissa indicates the relative outward distance.

658

659